ACS OMEGA

http://pubs.acs.org/journal/acsodf

Article

Material Design of Bimetallic Catalysts on Nanofibers for Highly Efficient Catalytic Reduction of 4-Nitrophenol

Daniel, Indra Masmur,* Sabarmin Perangin-angin, Subur P. Pasaribu, Agustina R. Magdaleni, Hestina, Helmina Br. Sembiring, Albert Pasaribu, and Elvri Melliaty Sitinjak

Cite This: *ACS Omega* 2023, 8, 17234−17244

Read Online

ACCESS | Metrics & More | Article Recommendations | Supporting Information

ABSTRACT: In this study, $CuO-TiO_2$ nanofiber catalysts were fabricated by an electrospinning process, followed by thermal annealing at various temperatures ranging from 300 to 700 °C. The phase transformation from CuO to metallic Cu was carried out through immersion treatment in $NaBH_4$ solution. The resulting $CuO-TiO_2$ and $Cu-CuO-TiO_2$ nanofibrous mats were characterized by scanning electron microscopy (SEM), transmission electron microscopy (TEM), X-ray photoelectron spectroscopy (XPS), X-ray diffraction (XRD), and Brunauer−Emmett−Teller (BET) analysis. The results revealed that the crystalline phase composition of the nanofibrous mats considerably affected the efficiency of photocatalytic reduction, where the $CuO-TiO_2$ catalysts with a predominant anatase content was found to be more photoactive than the rutile phase. Similarly, the presence of both Cu and CuO species was more beneficial for promoting the activity of fibers by acting as an interim location for facilitating the electron transfer. The fabricated $Cu-CuO-TiO_2$ nanofibrous mat with a ratio presented high conversion (~99%) within several minutes with the apparent pseudo-first-order rate constant of 0.42 and 0.50 min^{-1} in the absence and presence of UV light irradiation as well as excellent stability in recycling runs with a stable conversion efficiency of 97% or higher over five successive catalytic cycles.

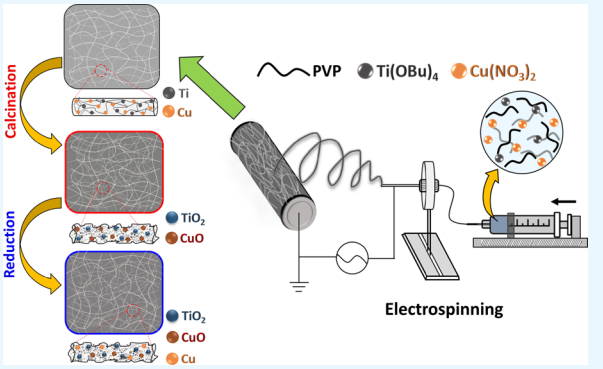

1. INTRODUCTION

Polluted freshwater resources remain as one of the global challenges in this century, which directly impact the environment and economy. Among the organic pollutants contained in polluted water, nitroaromatic compounds are found to be the most common and severely toxic chemicals because of their highly stability, water solubility,[1] and carcinogenic effects even at low concentrations.[2,3] An example of nitroaromatic compounds is 4-nitrophenol (4-NP), which is categorized as a toxic pollutant by the Environmental Protection Agency, with a limit concentration of 1−20 ppb[1]. 4-NP has been widely used particularly for industrial applications (e.g., dyestuff, pesticide, explosives, etc.). The negative effects of nitrophenol exposure on human are dizziness, skin irritation, and organ disfunction. Furthermore, the presence of this toxic organic chemical in water bodies could harm the marine biota, which further bring the domino-effect to humans through the food chain.[4] Therefore, there has been a tremendous number of efforts dedicated to purify the contaminated water and wastewater to ensure a clean and healthy environment. Several methods are currently employed to remove nitrophenol in water bodies such as photolysis, electrolysis, adsorption, and Fenton reaction.[5−7] However, most of the aforementioned techniques are restricted for practical applications with low efficiency. Catalytic reduction approach has drawn attention from researchers owing to its highly efficient and large-scale process to convert 4-NP to 4-aminophenol (4-AP) on a nanostructured catalyst and is considered to be sustainable and economically friendly as well. Hence, materials design with high specific surface area, active sites, and robust durability is required to be developed.[8]

In the past few decades, the development of nanomaterials particularly for reduction of 4-NP to 4-AP involved a nanosized noble metal,[9−11] carbon-based materials,[12,13] and transition metals.[14,15] Specifically, bimetallic materials provide superior catalytic performances arising from their synergetic combination of two kinds of metals. For instance, Pt−Ni bimetallic possesses better catalytic activity and corrosion resistance as compared to Pt metallic alone for 4-NP reduction assisted with $NaBH_4$.[16] Pozun et al. reported a higher reaction rate constant of bimetallic dendrimer encapsulated nano-

Received: March 14, 2023
Accepted: April 25, 2023
Published: May 4, 2023

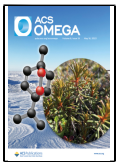

particles (DENs), where two metals were alloyed to trigger faster reaction rates as compared to their monometallic catalysts.[17] Regardless, previous works suffer from the expensive noble metal price and have serious issues for commercial production. Thus, the utilization of transition metals to replace noble metals not only would benefit economically but is also potential for large-scale production. As for the transition metal, copper is a good choice since Cu is an abundant resource and a highly active element with varied oxidation states.[18] Another candidate is accompanied by titanium; Ti is a low-cost material, highly stable, and strong oxidizer.[19] Furthermore, the improvement in terms of reusability purpose could be applied by embedding the bimetallic catalysts into a nanofibrous structure material, which also enhances the surface area due to its highly porous network.[20]

To date, no studies reported the synthesis of the copper-titania bimetallic catalyst on nanofibers with tunable phase compositions for catalytic reduction of 4-NP to 4-AP. With this regard in mind, a material design of copper−titania (Cu−Ti) bimetallic embedded in PVP nanofibers was synthesized by electrospinning process followed by reduction reaction. The as-prepared nanofibrous bimetallic catalyst was applied for catalytic reduction of 4-NP to 4-AP. In addition, the kinetics and thermodynamics of Cu−Ti bimetallic nanofibrous catalysts are thoroughly discussed in this study.

2. MATERIALS AND METHODS

2.1. Chemicals. PVP (MW = 40,000 g/mol), sodium borohydride ($NaBH_4$, 98%), 4-NP (Echo chemicals, 99%), copper(II) nitrate trihydrate ($Cu(NO_3)_2{\cdot}3H_2O$, Sigma Aldrich, 99.5%), and tetrabutyl titanate (TT, Sigma Aldrich, 97%) were used as received without any purification.

2.2. Preparation of Cu−Ti Bimetallic Nanofibers. In a typical experiment, the Cu−Ti bimetallic nanofibrous catalyst was fabricated by mixing $Cu(NO_3)_2$ and TT-PVP as copper and titanium sources, respectively. The titanium precursor solution was prepared via a sol−gel method by stirring ethanol, acetic acid, and TT at an ambient temperature for min. Subsequently, 2 g of PVP was added and stirred until homogeneous. Then, $Cu(NO_3)_2$ solution in ethanol was added into TT-PVP solution. The resulting viscous solution was transferred to a plastic syringe equipped with a stainless steel blunt-ended needle. Electrospinning was conducted at 20 kV, with a speed rate of 0.01 mL/h and a distance of 15 cm between the tip of the needle and drum collector. The as-obtained nanofibers were then stored in an electric oven at 65 °C to avoid moisture and later used for further characterizations. The formulation of different copper and titanium precursors is tabulated in Table 1 and abbreviated as T_nC_m, where n and m represent the concentrations of titanium and copper precursors, respectively.

The thermal crosslinking process of T_nC_m PVP nanofibers was carried out at 180 °C for 3 h in an electric muffle furnace under air atmosphere. T_nC_m PVP nanofibers were further annealed at 300−700 °C for 30 min with a heating ramp of 10 °C/min. The annealed nanofiber products were named as T_nC_m-X, where X denotes the annealing temperature. To reduce Cu^{2+} to metallic cupper (Cu^0), T_nC_m-X nanofibers were simply immersed in $NaBH_4$ solution at different immersion times and the samples were named as T_nC_m-X_r, where r represents the reduction time.

Table 1. Composition of Electrospinning Copper-Titanium Bimetallic Nanofibers

	solution composition		
samples	TT (wt %)	$Cu(NO_3)_2$ (wt %)	Ø (nm)
T_6C_1	6	1	508 ± 143
T_3C_1	3	1	655 ± 74
T_1C_1	1	1	344 ± 70
T_1C_3	1	3	760 ± 220
TT-PVP	6		426 ± 67

2.3. Materials Characterizations. The surface morphology of the prepared nanofibers was observed using field emission scanning electron microscopy (FE-SEM, JEOL JSM-7900) with an accelerating voltage of 30 kV equipped with an energy dispersive X-ray (EDX) detector for elemental composition and transmission electron microscopy (TEM, JEOL 2000FX). The crystallinity and phase identification of samples were examined using X-ray diffraction (XRD, Bruker D2 Phaser) and X-ray photoelectron spectroscopy (XPS, ESCALAB 250) analyses. Inductively-coupled plasma atomic emission spectra (ICP-AES, Shimadzu ICPE-9800) analysis was used to determine the titanium and copper content in the obtained nanofibers. The surface area of the heterogeneous catalyst was further studied by BET analysis.

2.4. Catalytic Experiments. The catalytic performances of bimetallic nanofibers were evaluated at dark and UV-light irradiated conditions. In a typical experiment, ∼2 mg of bimetallic nanofibers was dispersed in 4-NP solution with a concentration of 0.5 mM. Prior to photocatalytic reaction, the dispersion was stirred for 30 min under dark conditions to reach the adsorption−desorption equilibrium. Afterward, 5 mL of 0.1 M $NaBH_4$ was dropwise added and, at the same time, irradiated with UV light while stirring. The aliquot was taken after a certain period of time and further analyzed using a UV−vis spectrophotometer (Jasco V-650). The reusability performances of bimetallic nanofibers were also tested on five consecutive cycle experiments.

2.5. Kinetic and Thermodynamic Analysis. The kinetics of catalytic and photocatalytic 4-NP reduction reaction in the presence of bimetallic nanofibers were studied by monitoring the changes in absorbance of 4-nitrophenolate ions at λ_{max} = 400 nm at different time intervals. In this model reaction, the kinetics of 4-NP reduction in the presence of excess $NaBH_4$ can be assumed to follow a pseudo-first-order model. The reaction rate constant with respect to 4-nitrophenolate ions can be expressed as follows (eq 1):

$$-\ln\left(\frac{C_t}{C_0}\right) = -\ln\left(\frac{A_t}{A_0}\right) = k_t \tag{1}$$

where A_t and A_0 refer to the absorbance of 4-nitrophenolate ions at times t and 0, respectively, while C_t and C_0 are the equivalent concentrations of the same species at times t and 0, respectively. The apparent rate constant (k_{app}) can be obtained from the slope of the linear plot of $-\ln(A_t/A_0)$ versus time.

The thermodynamic aspect of the reaction, such as predicting the apparent activation energy (E_a), the enthalpy of activation ($\Delta H^{\ddagger}$), and the Gibbs energy of activation ($\Delta G^{\ddagger}$), was investigated by conducting the 4-NP reduction experiments at different temperatures (i.e., 303, 313, and 323 K). The E_a (kJ mol^{-1}) can be calculated from the slope of the Arrhenius plot describing a linear relationship between the

https://doi.org/10.1021/acsomega.3c01285
ACS Omega 2023, 8, 17234−17244

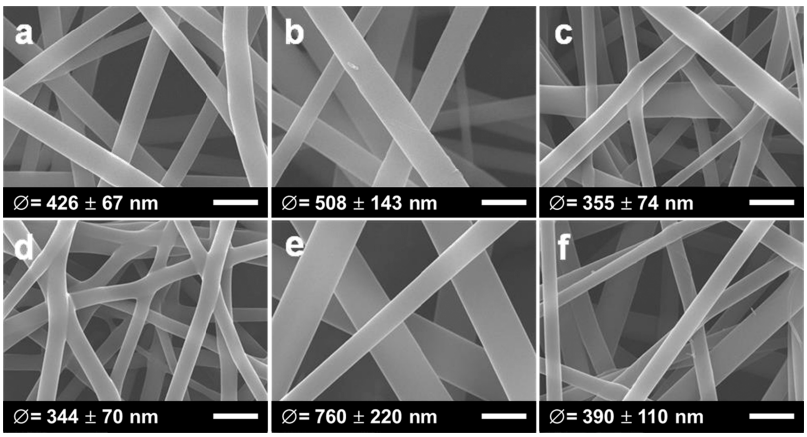

Figure 1. SEM images of as-spun fibers of (a) TT-PVP, (b) T_6C_1, (c) T_3C_1, (d) T_1C_1, (e) T_1C_3, and (f) Cu-PVP. The scale bar in all figures is 1 μm.

logarithm of the rate constant (k_{app}) and the inverse of absolute temperature ($1/T$) according to the following equation (eq 2):

$$\ln k_{app} = -\frac{E_a}{RT} + \ln A \tag{2}$$

where R and A denote the universal gas constant (8.314 J mol^{-1} K^{-1}) and pre-exponential factor related to the steric effect and collision frequency, respectively. The values of the enthalpy and entropy of activation ($\Delta S^{\ddagger}$) can be obtained from the Eyring equation (eqs 3 and 4), describing a linear relationship between the reaction rate and temperature:[21]

$$\ln\left(\frac{k_{app}}{T}\right) = \frac{-\Delta H}{R}\frac{1}{T} + \ln\left(\frac{k_B}{h}\right) + \frac{\Delta S}{R} \tag{3}$$

$$\Delta G^{\ddagger} = \Delta H^{\ddagger} - T\Delta S^{\ddagger} \tag{4}$$

where k_B and h are the Boltzmann's (1.38×10^{-23} J K^{-1}) and Planck's constant (6.63×10^{-34} J s), respectively.

3. RESULTS AND DISCUSSION

3.1. Morphology of Bimetallic Nanofibers. The surface morphology of T_nC_m PVP nanofibers is shown in Figure 1. From this figure, it can be seen that all the fibers exhibited a smooth and uniform surface without discernable bead defects. The average diameter of T_nC_m PVP nanofibers was found to be affected by the precursor solution composition, particularly the titanium-to-copper ratio. The addition of metal salt into the polymer solution was also reported to affect the spinnability of the polymer jet since it will increase the number of ions and conductivity. Generally speaking, a more conductive and viscous solution results in the formation of a thinner nanofiber. In this regard, the average diameter of the T_nC_m PVP nanofibers decreased from 508 ± 143 to 355 ± 74 and 344 ± 70 nm with a decreasing titanium content in the solution (T_6C_1 to T_1C_1); meanwhile, it is bigger in size with increasing copper content (T_1C_3), which might be due to hygroscopic properties of copper nitrate precursors. As can be seen in Table 2, the average diameter of as-spun nanofibers was varied in between 94 and 513 nm. Moreover, BET results showed aT-400 possesses surface area of 173.1 m^2 g^{-1}, pore volume of 19.6, and pore size of 3.1 nm. The surface area, pore volume, and pore size of nanofiber catalysts gradually decreased with a decreasing Ti concentration (T_6C_1 to T_1C_1) as shown in Table S1. Interestingly, the surface area, pore volume, and pore size of nanofiber significantly increased after reducing by $NaBH_4$ (T_1C_3-400_S).

Table 2. Average Diameter and Crystalline Phase Composition of T_nC_m-400 and T_nC_m-400_S Nanofiber Catalysts

			TiO_2 crystallinity	
catalyst	Ø (nm)	crystal phases	anatase (wt %)	rutile (wt %)
T-400	129 ± 28	TiO_2	83.7	16.3
T_6C_1-300	513 ± 59	amorphous	ND	ND
T_6C_1-400	189 ± 45		85.7	14.3
T_6C_1-500	313 ± 89	TiO_2	72.4	27.6
T_6C_1-600	204 ± 52		27.8	72.2
T_6C_1-700	273 ± 74		ND	100
T_3C_1-400	124 ± 28	TiO_2, CuO	83.4	16.6
T_1C_1-400	175 ± 42		86.2	13.8
T_3C_1-400	201 ± 87	TiO_2	85.4	14.6
T_6C_1-400_S	203 ± 23		85.0	15.0
T_3C_1-400_S	94 ± 23	TiO_2, CuO, Cu	81.0	19.0
T_1C_1-400_S	91 ± 23		83.6	26.4
T_1C_3-400_S	223 ± 59		100	ND

Figure 2 depicts the morphology of T_nC_m PVP nanofibers annealed at 400 °C. From this figure, it can be seen that all the annealed fibers had a significantly smaller diameter than the precursor fibers, which could be attributed to the thermal decomposition of the polymer matrix. Previous reports have shown that PVP decomposes upon heating in the air at temperatures between 350 and 400 °C.[22,23] The formation of such metal oxide agglomerates can be ascribed to the activation and diffusion-controlled neck growth of Ti and Cu atoms by thermal energy. This also suggests that thermal annealing at 400 °C can induce the formation of crystalline metal oxide phases (i.e., TiO_2 and CuO); both of which are beneficial for catalytic reactions. Additionally, one can also notice that Cu nanoparticles are uniformly decorated on the surface of T_nC_m–400_S nanofibers prepared from electrospinning solutions with higher concentrations of copper salt, providing more catalytic active sites for 4-NP reduction. Furthermore, TEM analysis shows that the nanostructure of T_1C_3 (without annealing) was found to be agglomerated as shown in Figure 2m. These agglomerates then become slightly separated after annealing, T_1C_3-400 (Figure 2n), and after reducing by $NaBH_4$, the

https://doi.org/10.1021/acsomega.3c01285
ACS Omega 2023, 8, 17234−17244

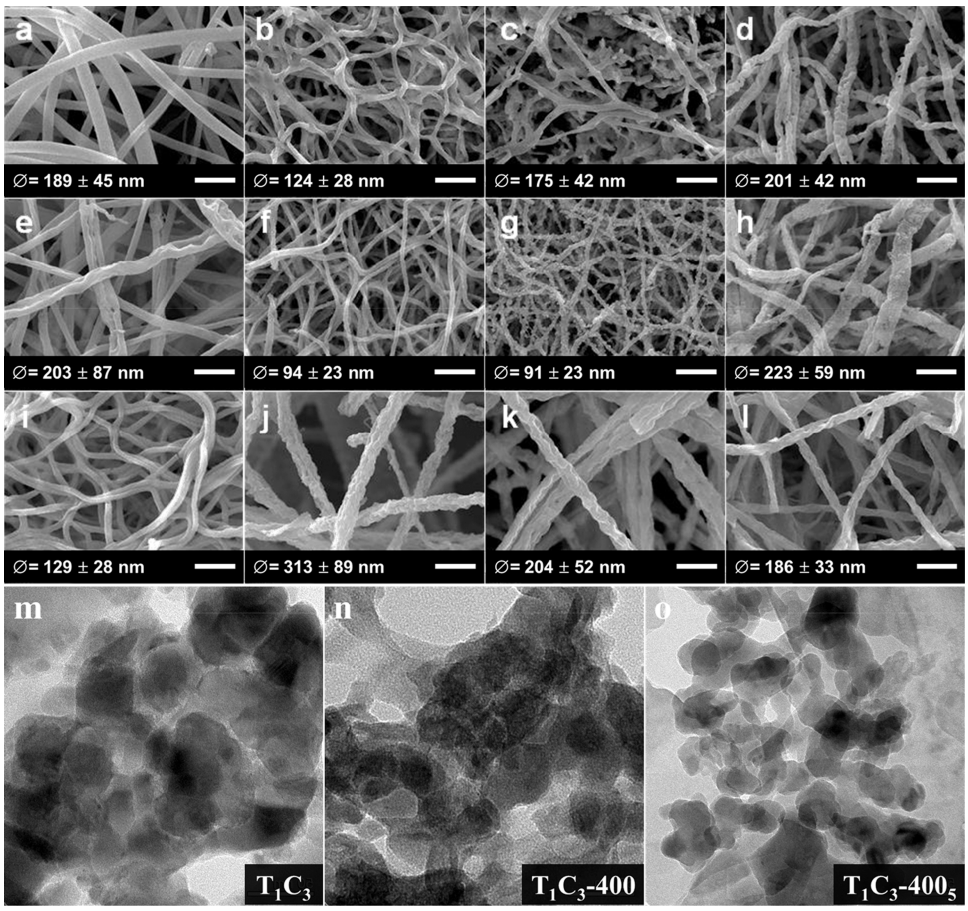

Figure 2. SEM images of annealed T_nC_m PVP nanofiber; (a) T_6C_1, (b) T_3C_1, (c) T_1C_1, and (d) T_1C_3. SEM micrographs (e–h) of the nanofibrous mats corresponding to panels a-d after immersion in $NaBH_4$ solution for 5 min to reduce CuO to metallic Cu. SEM images of (i) T-400 nanofiber and T_6C_1 nanofibers annealed at (j) 500 °C, (k) 600 °C, and (l) 700 °C. TEM images of (m) T_1C_3, (n) T_1C_3-400, and (o) T_1C_3-400_5 nanofibers. The scale bar for SEM images represents 1 μm.

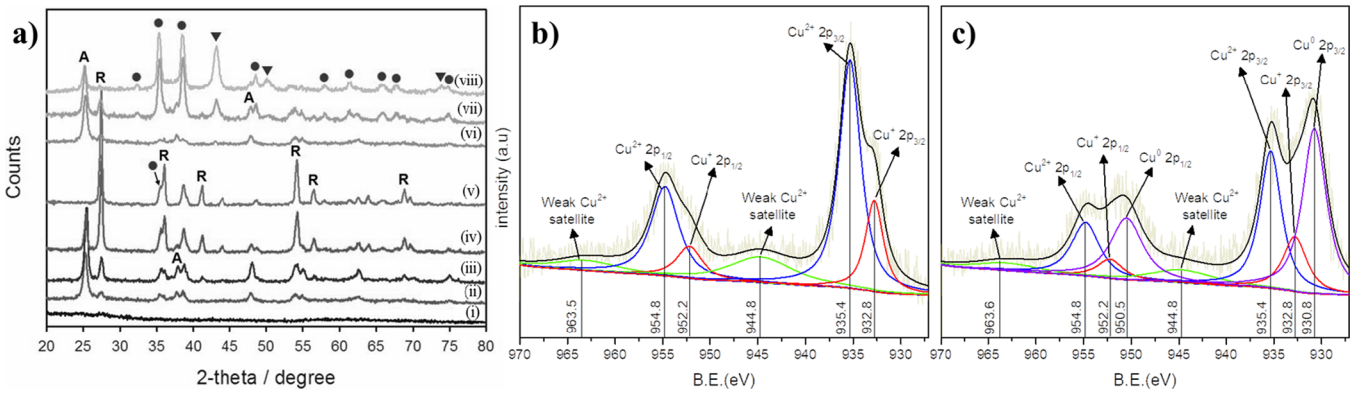

Figure 3. (a) Wide angle XRD patterns of the T_6C_1 nanofiber annealed at (i) 300, (ii) 400, (iii) 500, (iv) 600, and (v) 700 °C; (vi) T_6C_1, (vii) T_1C_1, and (viii) T_1C_3 nanofibers after being annealed at 400 °C for 30 min and immersed in $NaBH_4$ solution for 5 min. Diffraction peaks corresponding to the anatase TiO_2, rutile TiO_2, CuO, and metallic Cu phases are denoted by "A", "R", circles, and triangles, respectively. High-resolution XPS spectra of the Cu element in (b) T_1C_3-400 and (c) T_1C_3-400_5 nanofibers.

obtained particles were of irregular shape without any agglomeration with the average size of 20–30 nm as can be seen in Figure 2o. In addition, the elemental composition of T_1C_3-400 and T_1C_3-400_5 nanofibers was analyzed by EDX analysis as the representatives of CuO–TiO_2 and Cu–CuO–TiO_2 crystal phases as shown in Figure S1. The EDX spectra showed that the atomic percentage of O decreased after reducing using $NaBH_4$ from 17 to 14.2%, and the amount of Ti and Cu slightly increased, indicating that CuO in T_1C_3-400 was transformed into Cu^0 in T_1C_3-400_5.

3.2. Crystal Phase and Composition of the Bimetallic Nanofibrous Mats. The XRD patterns of the fabricated bimetallic nanofibrous mats are presented in Figure 3. As can be seen in the figure, there are no characteristic Bragg reflections associated with the crystal structures of TiO_2 and copper oxides for the T_6C_1-300 sample, indicating the

https://doi.org/10.1021/acsomega.3c01285
ACS Omega 2023, 8, 17234–17244

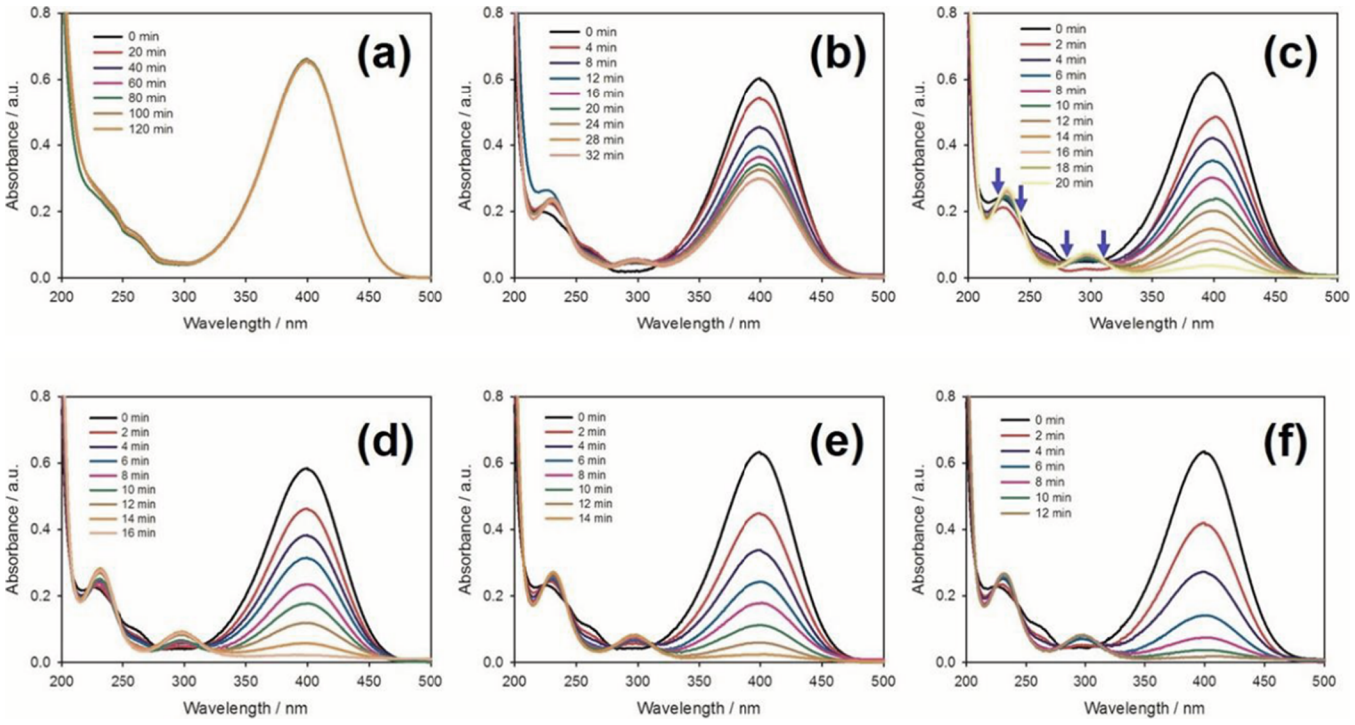

Figure 4. Time-dependent UV−vis absorption spectra of the reaction mixture consisting of 4-NP (0.2 mM), $NaBH_4$ (90 mM), and as-prepared nanofibrous catalysts, (a) crosslinked T_6C_1, (b) T-400, (c) T_6C_1-400, (d) T_3C_1-400, (e) T_1C_1-400, and (f) T_1C_3-400, under UV irradiation. The blue arrows in panel (c) indicate representative four isosbestic points at 227, 244, 281, and 314 nm.

amorphous nature of the fibers. On the contrary, the XRD patterns of T_6C_1-400, T_6C_1-500, T_6C_1-600, and T_6C_1-700 nanofibers contain several sharp and intense Bragg reflections corresponding to the TiO_2 polymorphs following thermal annealing at higher temperatures. The assignment of the crystalline phases was based on the reference files Joint Committee on Powder Diffraction Standards (JCPDS) No. 21-1272, No. 21-1276, No. 45-0937, and No. 04-0836 for anatase TiO_2, rutile TiO_2, CuO, and metallic Cu, respectively. On the other hand, there is a tiny peak assigned for Cu_2O observed at 44° after T_6C_1 annealed at 600 and 700 °C as can be seen in Figure 3iv,v. The results demonstrate that the formation of the two crystalline phases strongly depends on the annealing temperature,[17,24] where T_6C_1-400, T_6C_1-500, and T_6C_1-600 samples exhibited a mixed anatase-rutile phase and the T_6C_1-700 sample comprised only the rutile phase (Table 2). Meanwhile, no appreciable copper oxide species could be observed in the XRD patterns of these samples probably because of low concentration and also because the main reflections of copper oxides overlap those of anatase and rutile TiO_2. Panels (vi), (vii), and (viii) show the diffraction patterns of T_6C_1-400, T_1C_1-400, and T_1C_3-400 nanofibers after immersion treatment in $NaBH_4$ solution. In addition to reflections from TiO_2 polymorphs, new reflections associated to copper phases between 30° and 50° appear. Moreover, it can be observed that the Bragg peaks assigned to monoclinic CuO at 2θ become sharper and more intense in T_1C_1-400 and T_1C_3-400 nanofibers with a higher amount of copper loading. For all T_nC_m-X samples, no traces of the cubic Cu_2O phase were found, indicating the complete thermal oxidation of amorphous Cu to CuO ($2Cu + O_2 \rightarrow 2CuO$) under annealing treatment at 400 °C and beyond in air atmosphere. This phase transition is in good agreement with the results reported by De Los Santos Valladares et al.[25] Thus, it can be implied that the coexistence of both active TiO_2 with a predominant anatase phase and copper/copper oxide phases on T_nC_m-X nanofibers is beneficial for facilitating catalytic reduction of 4-NP to 4-AP.

Furthermore, Figure 3b,c shows the high-resolution XPS spectra of the Cu element in T_1C_3-400 and T_1C_3-400_S nanofibers. Both XPS spectra exhibited Cu^+ $2p_{3/2}$, Cu^+ $2p_{1/2}$, Cu^{2+} $2p_{3/2}$, and Cu^{2+} $2p_{1/2}$ peaks located at 932.8, 952.2, 935.4, and 954.8 eV, respectively, and were also accompanied by their satellite peaks of Cu^{2+} at 944.8 and 963.5 eV.[26] By comparing the peak intensity in Figure 3b,c, the peaks for Cu^{2+} and Cu^+ including the satellite peaks decreased after reduction using $NaBH_4$.[27] Also, there is one additional set of Cu^0 2p peaks located 930.8 and 950.5 eV in the T_1C_3-400_S nanofiber (Figure 3c), Therefore, this phenomenon successfully revealed that Cu^{2+} in T_1C_3-400 was converted to Cu^0 in the T_1C_3-400_S nanofiber.

3.3. Photocatalytic Activities of Bimetallic Nanofibers. The catalytic and photocatalytic activities of the fabricated electrospun samples were evaluated for reduction reaction of 4-NP to 4-AP in the aqueous phase at room temperature. The pH of the 4-NP solution before and after the addition of $NaBH_4$ was measured using a microelectrode pH meter and found to be around 7.2 and 9.6, respectively. In this model reaction, the reduction of 4-NP by BH_4^- does not occur in the absence of the catalyst since there was neither color change from yellow to transparent observable by naked eyes nor a gradual decrease in the absorbance maxima of 400 nm corresponding to 4-nitrophenolate ions with time. Similar results were observed for the T_6C_1 sample with amorphous copper and TiO_2 phases as the catalyst, showing negligible photocatalytic activity (Figure 4a). The pure anatase-rich TiO_2 nanofiber shows a rather moderate catalytic activity toward 4-NP reduction, where only ~50% conversion was achieved after 32 min (Figure 4b). On the contrary, T_nC_m-400 nanofibers

https://doi.org/10.1021/acsomega.3c01285
ACS Omega 2023, 8, 17234−17244

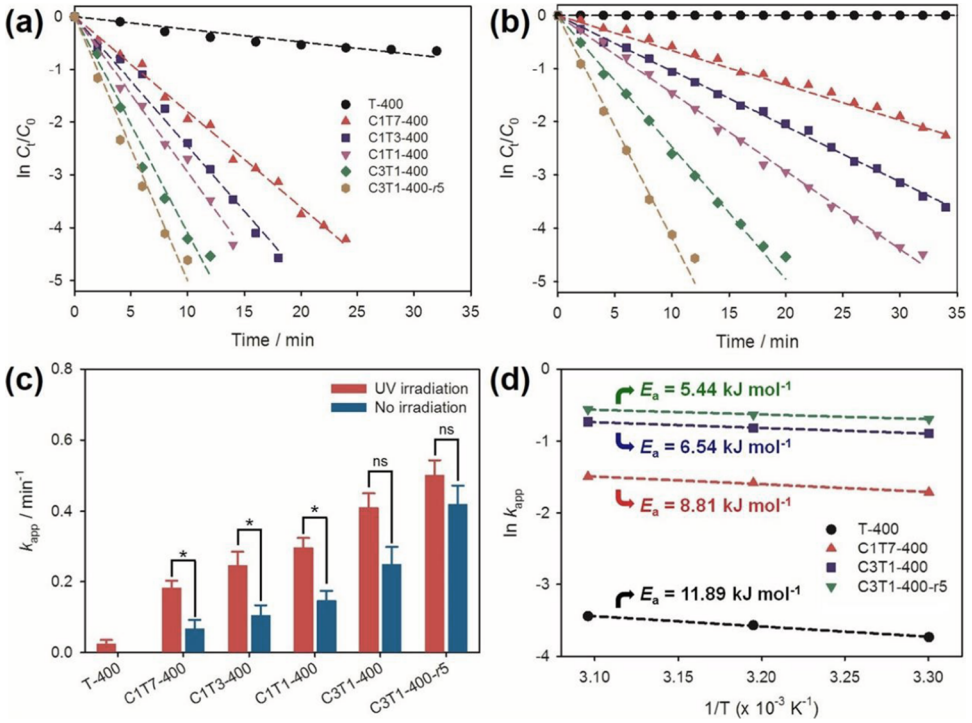

Figure 5. Pseudo-first-order kinetic plots of the 4-NP reduction catalyzed by different nanofibrous mats (a) with and (b) without UV irradiation. The legend in (a) also applies to panel (b). The correlation fitted by eq 1. is shown as colored dashed lines in panels (a) and (b). (c) Bar plot showing the comparisons of the k_{app} values for catalytic reduction of 4-NP in the presence and absence of UV exposure. Bars represent the mean value, and error bars show the standard error of the mean from three independent experiments (n = 3). Asterisk (*) and 'ns' denote statistical significance at $P < 0.05$ and no statistical significance, respectively, based on unpaired two-tailed Welch's t-test using GraphPad Prism v6.01 software. (d) Arrhenius plots for photocatalytic 4-NP reduction by T-400, T_6C_1-400, T_1C_3-400, and T_1C_3-400_5 nanofibers. The E_a values are equal to the negative slopes of the respective linear fits multiplied by R (8.314 J mol^{-1} K^{-1}) over three temperatures (303, 313, and 323 K).

with different bimetallic compositions and crystalline phases demonstrate high photocatalytic activity for 4-NP reduction, as shown in Figure 4c–f. As can be seen from these figures, the complete conversion of 4-NP to 4-AP was achieved after 10–20 min of reaction at room temperature without formation of side products, as confirmed by two isosbestic points at 280 and 314 nm.[12] The results also indicate that the nanofibrous mats with higher Cu/Ti ratios, for example, T_1C_1-400 and T_1C_3-400, demonstrate higher efficiency toward 4-NP reduction than the T_6C_1-400 sample, which might be attributed to the presence of the CuO phase. In this regard, the CuO phase acts as a 'shuttle bus' to enhance separation efficiency of the photogenerated electrons (e_{cb}^-) and holes (h_{vb}^+) by forming a p–n heterojunction interface with the electron-rich (101) facet of TiO_2. A similar synergistic effect of photogenerated charge separation in the CuO–TiO_2 heterojunction was observed for selective photo-oxidation of methanol to methyl formate[28] and degradation of 2,4-dichlorophenoxyacetic acid.[29] In addition, the positively charged CuO embedded in the surface of fiber catalysts may facilitate the adsorption of negatively charged 4-NP and hydrolyzed borohydride molecules on the surface through electrostatic interactions, leading to the elimination of the induction period and increased reaction efficiency.[30] Since both copper and copper oxide phases in T_6C_1-X nanofibers were hardly recognized from the XRD results (Figure 3, panels a–e), it can be implied that the photocatalytic activities of these samples are mainly contributed by the TiO_2 polymorphs. The results show that the photocatalytic activity of the fibers becomes lower when the samples were annealed at higher temperatures, suggesting that the anatase T_6C_1 nanofiber catalyst is more active than its rutile counterpart toward 4-NP reduction. The k_{app} value of T_6C_1-400 was about 2-fold higher compared to that of the T_6C_1-700 sample. Similarly, Sclafani and Herrmann[31] and Tanaka et al.[32] reported better photocatalytic performance of TiO_2 nanoparticles with a higher anatase-to-rutile ratio for the degradation of organics in aqueous solutions. This can be attributed to the more negative conduction band energy minima of anatase that allows for a more facile electron transfer process to 4-NP and a lower recombination velocity of e_{cb}^- and h_{vb}^+ as well as a stronger adsorption affinity of 4-NP molecules toward the anatase (101) surface compared to that on the rutile (110) surface.[33] The latter factor is thought to play a major role in the process since the reduction of 4-NP involves a key step in which the electron was transferred from donor BH_4^- to the acceptor 4-NP.[8,34] Moreover, the existence of a minor rutile phase in the T_6C_1-400 sample may also be beneficial for the separation of photogenerated charge carriers since h_{vb}^+ will preferentially move to rutile owing to its higher valence band maximum energy.[25,35] Therefore, an annealing temperature of 400 °C was chosen in this study to prepare photoactive anatase T_nC_m nanofibrous catalysts for subsequent catalytic testing and $NaBH_4$ reduction experiments. In addition, the use of a lower annealing temperature is energetically more feasible for large-scale manufacturing of this nanofibrous catalyst.

3.3.1. Effects of the Copper Phase Compositions. The photocatalytic activities of the anatase T_nC_m-400 nanofibers with the pure CuO phase and the mix phase Cu–CuO are shown in Figure 5. The formation of a mixed Cu–CuO phase was carried out through immersion in $NaBH_4$, which allows

https://doi.org/10.1021/acsomega.3c01285
ACS Omega 2023, 8, 17234–17244

Table 3. Apparent Pseudo-First-Order Rate Constants (k_{app}) for 4-NP Reduction with $NaBH_4$ at Room Temperature Catalyzed by Various Nanofibrous Mats in the Presence and Absence of UV Irradiation

samples		T-400	T_6C_1-400	T_3C_1-400	T_1C_1-400	T_1C_3-400	T_1C_3-400$_5$
k_{app} (min^{-1})	UV	0.024	0.181	0.246	0.295	0.410	0.500
	no irradiation		0.066	0.104	0.146	0.248	0.419
t_{99}-UV (min)[a]	experimental		≈26	≈18	≈14	≈12	≈10
	prediction RSE	191.9	25.4	18.7	15.6	11.2	9.2

[a] t_{99} represents the time required to achieve a 99% conversion for 4-NP. RSE was calculated from the difference between experimental and predicted values.

the reduction of CuO to Cu with H_2 according to stoichiometric reactions. To explore the effect of immersion time of the C_xT_y-400 substrates in the $NaBH_4$ aqueous solution, the photocatalytic reduction activity of these substrates after the immersion treatments for 1, 5, and 10 min was evaluated. From our experiments, the optimized reduction time by $NaBH_4$ solution was found to be 5 min. From Figure 5a,b, it can be shown that the T_nC_m-400$_5$ nanofiber catalysts exhibited better catalytic performance compared to T_nC_m-400 containing only the CuO phase. The superior photocatalytic activity of the T_nC_m-400$_5$ nanofiber might be attributed to the copresence of CuO and Cu active phases, leading not only to an enhanced charge carrier separation generated from the CuO−TiO_2 heterojunction but also a more efficient electron transfer between the adsorbed BH_4^- and 4-NP molecules on the photocatalyst surface, which was facilitated by the high electrical conductivity (5.8×10^7 S m^{-1}) of copper.[36] The presence of copper as a cocatalyst can also help suppress the recombination of the photoexcited electron−hole pairs in the TiO_2 photocatalytic system because some e_{cb}^- of TiO_2 could transfer directly to the Cu by ohmic interconnection.[37] Moreover, metallic Cu embedded in the surface of the fibers can also serve as active sites to react with hydride (H^+) ions generated from spontaneous hydrolysis of BH_4^-, which upon contact with the catalyst surface donate its electrons to Cu and then combine to form H_2 gas.

3.3.2. Effects of UV Irradiation. The effect of UV irradiation on the catalytic activity of T_nC_m-400 and T_nC_m-400$_5$ nanofibers is shown in Figure 5a,b. From this figure, it can be seen that the reduction of 4-NP to 4-AP by T_6C_1-400, T_3C_1-400, T_1C_1-400, and T_1C_3-400 nanofiber catalysts was promoted under UV illumination. A complete conversion of 4-NP to 4-AP was achieved in shorter periods of time, within 5−10 min, compared to reactions without light irradiation. A similar trend was observed for the T_nC_m-400$_5$ nanofiber catalysts with the ternary Cu−CuO−TiO_2 phase. The reason for the promotion effect of the UV light treatment is due to the generation of charge carriers in TiO_2 and CuO, where the photogenerated electrons serve as an additional source of electrons to reduce 4-NP, together with efficient electron relay and separation. Interestingly, T_1C_1-400 and T_1C_3-400 catalysts and their reduced samples still showed decent catalytic activity in catalyzing reduction of 4-NP without UV irradiation. As can be seen from the bar graph in Figure 5c, the effect of UV irradiation becomes insignificant in these nanofibrous catalysts since the obtained k_{app} values for reactions with and without UV irradiation are comparable and they were not significantly different ($P > 0.05$) based on the unpaired t test. The remarkable catalytic activity of T_1C_1-400$_5$ and T_1C_3-400$_5$ samples could be attributed to the effective adsorption of 4-NP and borohydride anions on the Cu−CuO−TiO_2 catalytic surface, which bears positively charged CuO and a rapid interfacial electron transfer from donor BH_4^- to acceptor 4-NP via the Cu mediator. It is also worth noting that the T-400 sample composed of pure anatase gave no 4-NP conversion in the absence of UV irradiation, which implies that the reduction of 4-NP to 4-AP mediated by TiO_2 does not occur without the formation of photogenerated charge carriers.

3.3.3. Kinetic Analysis of the 4-NP Reduction Reaction. Both catalytic and photocatalytic reduction of 4-NP to 4-AP in the presence of excess $NaBH_4$ were assumed to follow pseudo-first-order kinetics, and the corresponding kinetic plots of ln (C_t/C_0) versus time are depicted in Figure 5. As can be seen, a good fit between experimental data and the kinetic model was obtained, which is confirmed by the coefficient of determination (R^2) values greater than 0.98. Table 3 summarizes the obtained k_{app} values of the as-prepared nanofibrous catalysts in this study.

It is noted that the k_{app} values of T_nC_m-400$_5$ nanofiber samples are higher than those obtained for T_nC_m-400 samples, and more interestingly, the difference in the rate constant values becomes greater (about fold) as the amount of copper loading in the catalyst increases. This result once again stresses the importance of the metallic copper phase on the catalytic solid surface to facilitate rapid interfacial electron transfer between 4-NP and BH_4^- anions. Among the fabricated nanofibrous catalysts, the T_1C_3-400$_5$ nanofiber sample exhibited the highest catalytic activity toward 4-NP reduction, with the k_{app} values of 0.50 and 0.42 min^{-1} for reactions with and without UV irradiation, respectively. The catalytic activity of the T_1C_3-400$_5$ nanofiber is also comparable with some other metallic and non-metal catalysts reported in the literature.[1,13,15,38,39] For convenience of catalytic performance comparison, the normalized kinetic parameter (k_n) proposed by Liu et al.[38] was used, which has the following mathematical expression (eq 5):

$$k_n(\text{mmol g}^{-1}\text{ min}^{-1}) = \frac{C_0}{m} \times k_{app} \quad (5)$$

where C_0, V, and m refer to the initial concentration of 4-NP (mM), volume of 4-NP solution (L), and mass of the catalyst (g), respectively.

The catalytic activity of the T_1C_3-400$_5$ nanofiber outperforms that of many other 4-NP reduction catalysts reported so far in the literature, giving relatively high k_n values of 1.89 and 2.25 mmol g^{-1} min^{-1} in the absence and presence of UV exposure. It is obvious that the catalysis performances are strongly influenced by the Cu content in the nanofiber catalyst, in which as the Cu content in the nanofiber increases, the k_{app} increases as shown by ICP results in Table S1. However, there is no significant alteration in the metal content between T_1C_3-400 and T_1C_3-400$_5$ nanofibers. Other than this, the excellent catalytic activity by T_1C_3-400$_5$ is also supported by the BET

https://doi.org/10.1021/acsomega.3c01285
ACS Omega 2023, 8, 17234−17244

Table 4. Thermodynamic Parameters of Activation for the Photocatalytic Reduction of 4-NP to 4-AP over Designated Nanofibrous Catalysts at Different Temperatures

catalysts	T/K	$\Delta G^{\ddagger}$/kJ mol^{-1}	$\Delta H^{\ddagger}$/kJ mol^{-1}	$\Delta S^{\ddagger}$/J mol^{-1} K^{-1}	R^2
T-400	303	54.64	9.29	−149.68	0.994
	313	56.13			
	323	57.64			
T_6C_1-400	303	53.59	6.21	−156.36	0.980
	313	55.15			
	323	56.71			
T_1C_3-400	303	51.09	3.94	−155.60	0.991
	313	52.64			
	323	54.20			
T_1C_3-400$_5$	303	49.40	2.85	−153.64	0.982
	313	50.94			
	323	52.48			

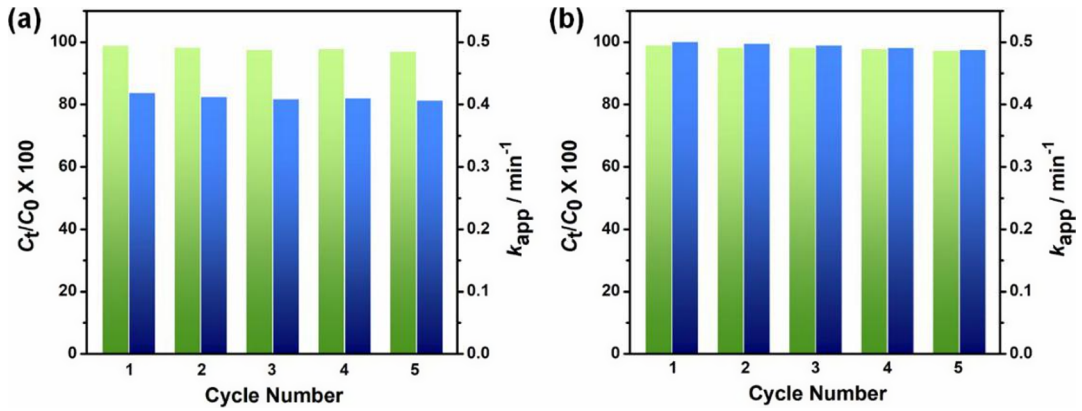

Figure 6. Cycling tests of (a) T_1C_3-400 and (b) T_1C_3-400$_5$ nanofibers for photocatalytic reduction of 4-NP to 4-AP over five cycles with respect to the apparent rate constant (k_{app}, blue bars) and conversion efficiency ($C_t/C_0 \times 100$, green bars).

results, which possesses the largest surface area, pore volume, and pore size. Compared with several noble metal-based composite nanocatalysts,[38−40] the present bimetallic catalytic system utilizing earth-abundant elements (Cu and Ti) exhibits a comparable or even better catalytic performance and, more importantly, is significantly cheaper in terms of metal price. In addition, the fabricated T_1C_3-400$_5$ nanofiber displayed superior activity for the reduction of 4-NP compared to the electrospun carbon nanofibers and PVDF nanofiber mats surface-decorated with silver nanoparticle-[41,42] and Pd nanoparticle-loaded cyclodextrin nanofibers.[42] Furthermore, the relatively straightforward and cost-effective fabrication method for the T_1C_3-400$_5$ nanofiber catalyst involving electrospinning, thermal annealing, and wet chemical reduction has the potential for upscaling and is likely to be adaptable for mass production.

3.3.4. Thermodynamic Analysis. The Arrhenius plots corresponding to several nanofibrous catalysts are given in Figure 5d. As can be seen in the figure, all the k_{app} values for photocatalytic 4-NP reduction increase with increasing reaction temperature, showing an endothermic nature of the reaction as expected. The slopes of the linear plots, which correspond to $-E_a/R$, are different in magnitude for each nanofibrous sample. The calculated E_a values for T-400, T_6C_1-400, T_1C_3-400, and T_1C_3-400$_5$ nanofiber catalysts were 11.89, 8.81, 6.54, and 5.44 kJ mol^{-1}, respectively. In this regard, the lowest E_a value was obtained for the 4-NP reduction reaction catalyzed by the T_1C_3-400$_5$ nanofiber and this correlates well with the faster transfer reaction that occurred on the catalyst surface. Moreover, all the E_a values are well within the typical reported values for the surface catalyzed processes (8.3−41.8 kJ mol^{-1}). From the point of view of liquid phase adsorption, it can be also inferred that the electrostatic interactions between anions and the catalyst surface belongs to physisorption. The calculated thermodynamic parameters of activation including $\Delta G^{\ddagger}$, $\Delta H^{\ddagger}$, and $\Delta S^{\ddagger}$ are presented in Table 4.

As it can be observed, the photocatalytic reduction of 4-NP to 4-AP was nonspontaneous ($\Delta G^{\ddagger} > 0$) and endothermic ($\Delta H^{\ddagger} > 0$); thus, this reaction requires energy or catalyst to promote the transformation of the reactant to product. Further, the value of $\Delta G^{\ddagger}$ becomes more positive with increasing temperature for all catalyst samples, indicating that the reduction of 4-NP becomes more facile and favorable at a lower temperature. The positive value of $\Delta G^{\ddagger}$ in this study also agrees well with the previous findings of Kohantorani and Gholami for catalytic reduction of 4-NP by CeO_2-supported CuNi nanoparticles[43] as well as for the Fenton-like photo-oxidation reaction.[44] The $\Delta H^{\ddagger}$ values, which represent energy differences between the ground state and the transition state in a chemical reaction, are consistent and follow the same trend as the E_a results: T_1C_3-400$_5$ < T_1C_3-400 < T_6C_1-400 < T-400. The decrease in the positive values of $\Delta H^{\ddagger}$ indicates that less energy would be required for the reaction to proceed to completion using the T_1C_3-400$_5$ nanofiber than the other nanofibrous samples. Meanwhile, the negative values of $\Delta S^{\ddagger}$ suggest loss of entropy due to a decrease in the randomness degree and the presence of an associative mechanism in forming the transition state for the catalytic reduction of 4-NP to 4-AP. This situation is frequently encountered in most

https://doi.org/10.1021/acsomega.3c01285
ACS Omega 2023, 8, 17234−17244

bimolecular reactions, where two reactant molecules (i.e., 4-NP and BH_4^-) come together on catalytic surfaces to form a product (4-AP). Thus, from the chemical thermodynamics' viewpoint, it can be implied that the T_1C_3-400_5 nanofiber was the best performing catalyst for facilitating the reduction of 4-NP to 4-AP, having the smallest E_a and $\Delta H^{\ddagger}$ values.

3.4. Reusability Test of the Nanofibrous Catalysts. The reusability and stability of the catalyst are important aspects to take into account for practical applications since they contribute toward lowering of the overall cost of the process. Therefore, the photocatalytic stability of T_1C_3-400 and T_1C_3-400_5 nanofibers was evaluated in five successive 4-NP reduction experiments. As can be seen in Figure 6 (panels a and b), the as-prepared T_1C_3-400 and T_1C_3-400_5 nanofibers displayed satisfactory photocatalytic stability with respect to the k_{app} values and conversion efficiency after five consecutive catalytic runs. In this regard, the k_{app} values do not significantly change compared to the original one, while the catalytic conversion efficiency remains constant at 97% or above across the five runs for both nanofibrous catalysts. Moreover, the nanofibrous morphology of T_1C_3-400 ($CuO-TiO_2$) and T_1C_3-400_5 ($Cu-CuO-TiO_2$) catalysts may also facilitate the separation process of these solids from the solution after reaction, for example, simply by filtration, compared to powdery catalysts that require tedious and time-consuming centrifugation/redispersion cycles. Table 5 shows the kinetic parameter of 4-NP conversion using different catalysts as reported previously. This work using the T_1C_3-400_5 nanofiber outperforms other catalysts for 4-NP reduction to 4-AP.

Table 5. Comparison with the State-of-the-Art Literature of 4-NP Conversion under Different Catalysts

materials	size (nm)	k_n (mmol g^{-1} min^{-1})	light source	ref
$Ag-TiO_2$	19	0.036	visible light	45
ZnO−NCP	100	0.0008	UV light	46
$NdPc_2-TiO_2$		0.008	UV light	47
$Pd-TiO_2$	7	0.432		48
CuO	20	2.343		49
$Fe_3O_4@SiO_2-Ag$	200	1.527		50
T_1C_3-400_5	20−30	2.251	UV light	[this work]

4. CONCLUSIONS

In summary, we have successfully demonstrated in this study the composition-controlled fabrication of bimetallic copper−titania nanofibrous mats via a combination of electrospinning and thermal annealing processes. XRD results confirm the coexistence of Cu, CuO, and TiO_2 crystalline phases in the nanofibrous catalysts after $NaBH_4$ immersion treatment; meanwhile, the conversion of Cu^{2+} to Cu^0 after reduction by $NaBH_4$ was successfully revealed by XPS results. Among the fabricated bimetallic nanofibrous catalysts, the T_1C_3-400_5 fiber mat with coexisting Cu, CuO, and TiO_2 phases was found to be the best performing catalyst toward 4-NP reduction reaction with and without UV irradiation, giving the k_{app} values of 0.50 and 0.42 min^{-1}, respectively. The excellent catalytic activity demonstrated by T_1C_3-400_5 could be attributed to the electron separations from CuO and efficient electron transfer by Cu species. In addition, T_1C_3-400_5 also exhibits the largest surface area, pore volume, and pore size among other nanofiber catalysts as indicated by BET results. Based on the thermodynamic analysis of the activation parameters, the photocatalytic reduction of 4-NP to 4-AP was endothermic and nonspontaneous, where the reaction was favored at a low enthalpy value with T_1C_3-400_5 as the catalyst. The as-fabricated T_1C_3-400_5 nanofibrous catalyst is also stable and proved to be reusable for five consecutive reaction cycles without appreciable loss in activity, affording 4-NP conversions of at least 97%. To this end, this free-standing and low-cost bimetallic nanofibrous catalyst demonstrates its commercial potential to be implemented in industrial water and wastewater treatment containing nitroaromatic compounds.

■ ASSOCIATED CONTENT

Supporting Information

The Supporting Information is available free of charge at https://pubs.acs.org/doi/10.1021/acsomega.3c01285.

Elemental composition by EDX analysis of T_1C_3-400 and T_1C_3-400_5 nanofibers; BET surface and pore size analysis for various composite nanofibers; and actual metal content in composite nanofibers determined by ICP-AES (PDF)

■ AUTHOR INFORMATION

Corresponding Author

Indra Masmur − *Department of Chemistry, Faculty of Mathematics and Natural Sciences, Universitas Sumatera Utara, Medan 20155, Indonesia;* orcid.org/0000-0001-7853-4764; Email: indramasmur@usu.ac.id, intar76@yahoo.com

Authors

Daniel − *Department of Chemistry, Faculty of Mathematics and Natural Sciences, Mulawarman University, Samarinda 75123, Indonesia*

Sabarmin Perangin-angin − *Department of Chemistry, Faculty of Mathematics and Natural Sciences, Universitas Sumatera Utara, Medan 20155, Indonesia*

Subur P. Pasaribu − *Department of Chemistry, Faculty of Mathematics and Natural Sciences, Mulawarman University, Samarinda 75123, Indonesia*

Agustina R. Magdaleni − *Department of Medicinal Education, Faculty of Medicine, Mulawarman University, Samarinda 75123, Indonesia*

Hestina − *Department of Chemistry, Universitas Sari Mutiara Indonesia, Medan 20123, Indonesia*

Helmina Br. Sembiring − *Department of Chemistry, Faculty of Mathematics and Natural Sciences, Universitas Sumatera Utara, Medan 20155, Indonesia*

Albert Pasaribu − *Department of Chemistry, Faculty of Mathematics and Natural Sciences, Universitas Sumatera Utara, Medan 20155, Indonesia*

Elvri Melliaty Sitinjak − *Department of Chemical Engineering, Politeknik Teknologi Kimia Industri, Medan 20228, Indonesia*

Complete contact information is available at: https://pubs.acs.org/10.1021/acsomega.3c01285

Notes

The authors declare no competing financial interest.

https://doi.org/10.1021/acsomega.3c01285
ACS Omega 2023, 8, 17234−17244

■ ACKNOWLEDGMENTS

The authors would like to thanks Mulawarman University and Universitas Sumatera Utara for the facilities and instrumentation to conduct the research.

■ REFERENCES

(1) Di Paola, A.; Augugliaro, V.; Palmisano, L.; Pantaleo, G.; Savinov, E. Heterogeneous photocatalytic degradation of nitrophenols. *J. Photochem. Photobiol., A* **2003**, *155*, 207−214.
(2) Kovacic, P.; Somanathan, R. Nitroaromatic compounds: Environmental toxicity, carcinogenicity, mutagenicity, therapy and mechanism. *J. Appl. Toxicol.* **2014**, *34*, 810−824.
(3) Purohit, V.; Basu, A. K. Mutagenicity of Nitroaromatic Compounds. *Chem. Res. Toxicol.* **2000**, *13*, 673−692.
(4) Zieris, F. J.; Feind, D.; Huber, W. Long-term effects of 4-nitrophenol in an outdoor synthetic aquatic ecosystem. *Arch. Environ. Contam. Toxicol.* **1988**, *17*, 165−175.
(5) Weavers, L. K.; Ling, F. H.; Hoffmann, M. R. Aromatic Compound Degradation in Water Using a Combination of Sonolysis and Ozonolysis. *Environ. Sci. Technol.* **1998**, *32*, 2727−2733.
(6) Dhorabe, P. T.; Lataye, D. H.; Ingole, R. S. Removal of 4-nitrophenol from aqueous solution by adsorption onto activated carbon prepared from Acacia glauca sawdust. *Water Sci. Technol.* **2015**, *73*, 955−966.
(7) Kavitha, V.; Palanivelu, K. Degradation of nitrophenols by Fenton and photo-Fenton processes. *J. Photochem. Photobiol., A* **2005**, *170*, 83−95.
(8) Zhang, K.; Suh, J. M.; Choi, J.-W.; Jang, H. W.; Shokouhimehr, M.; Varma, R. S. Recent Advances in the Nanocatalyst-Assisted $NaBH_4$ Reduction of Nitroaromatics in Water. *ACS Omega* **2019**, *4*, 483−495.
(9) Zeng, J.; Zhang, Q.; Chen, J.; Xia, Y. A Comparison Study of the Catalytic Properties of Au-Based Nanocages, Nanoboxes, and Nanoparticles. *Nano Lett.* **2010**, *10*, 30−35.
(10) Kästner, C.; Thünemann, A. F. Catalytic Reduction of 4-Nitrophenol Using Silver Nanoparticles with Adjustable Activity. *Langmuir* **2016**, *32*, 7383−7391.
(11) Islam, M. T.; Saenz-Arana, R.; Wang, H.; Bernal, R.; Noveron, J. C. Green synthesis of gold, silver, platinum, and palladium nanoparticles reduced and stabilized by sodium rhodizonate and their catalytic reduction of 4-nitrophenol and methyl orange. *New J. Chem.* **2018**, *42*, 6472−6478.
(12) Kong, X.-K.; Sun, Z.-Y.; Chen, M.; Chen, C.-L.; Chen, Q.-W. Metal-free catalytic reduction of 4-nitrophenol to 4-aminophenol by N-doped graphene. *Energy Environ. Sci.* **2013**, *6*, 3260−3266.
(13) Wang, Z.; Su, R.; Wang, D.; Shi, J.; Wang, J.-X.; Pu, Y.; Chen, J.-F. Sulfurized Graphene as Efficient Metal-Free Catalysts for Reduction of 4-Nitrophenol to 4-Aminophenol. *Ind. Eng. Chem. Res.* **2017**, *56*, 13610−13617.
(14) Chinnappan, A.; Eshkalak, S. K.; Baskar, C.; Khatibzadeh, M.; Kowsari, E.; Ramakrishna, S. Flower-like 3-dimensional hierarchical Co_3O_4/NiO microspheres for 4-nitrophenol reduction reaction. *Nanoscale Adv.* **2019**, *1*, 305−313.
(15) Mandlimath, T. R.; Gopal, B. Catalytic activity of first row transition metal oxides in the conversion of p-nitrophenol to p-aminophenol. *J. Mol. Catal. A: Chem.* **2011**, *350*, 9−15.
(16) Ghosh, S. K.; Mandal, M.; Kundu, S.; Nath, S.; Pal, T. Bimetallic Pt−Ni nanoparticles can catalyze reduction of aromatic nitro compounds by sodium borohydride in aqueous solution. *Appl. Catal., A* **2004**, *268*, 61−66.
(17) Pozun, Z. D.; Rodenbusch, S. E.; Keller, E.; Tran, K.; Tang, W.; Stevenson, K. J.; Henkelman, G. A Systematic Investigation of p-Nitrophenol Reduction by Bimetallic Dendrimer Encapsulated Nanoparticles. *J. Phys. Chem. C* **2013**, *117*, 7598−7604.
(18) Gawande, M. B.; Goswami, A.; Felpin, F.-X.; Asefa, T.; Huang, X.; Silva, R.; Zou, X.; Zboril, R.; Varma, R. S. Cu and Cu-Based Nanoparticles: Synthesis and Applications in Catalysis. *Chem. Rev.* **2016**, *116*, 3722−3811.
(19) Ola, O.; Maroto-Valer, M. M. Review of material design and reactor engineering on TiO_2 photocatalysis for CO_2 reduction. *J. Photochem. Photobiol., C* **2015**, *24*, 16−42.
(20) Xue, J.; Xie, J.; Liu, W.; Xia, Y. Electrospun Nanofibers: New Concepts, Materials, and Applications. *Acc. Chem. Res.* **2017**, *50*, 1976−1987.
(21) Eyring, H. The Activated Complex and the Absolute Rate of Chemical Reactions. *Chem. Rev.* **1935**, *17*, 65−77.
(22) Koczkur, K. M.; Mourdikoudis, S.; Polavarapu, L.; Skrabalak, S. E. Polyvinylpyrrolidone (PVP) in nanoparticle synthesis. *Dalton Trans.* **2015**, *44*, 17883−17905.
(23) Li, R.-Z.; Hu, A.; Bridges, D.; Zhang, T.; Oakes, K. D.; Peng, R.; Tumuluri, U.; Wu, Z.; Feng, Z. Robust Ag nanoplate ink for flexible electronics packaging. *Nanoscale* **2015**, *7*, 7368−7377.
(24) Deng, J.; Wang, L.; Lou, Z.; Zhang, T. Design of CuO−TiO_2 heterostructure nanofibers and their sensing performance. *J. Mater. Chem. A* **2014**, *2*, 9030−9034.
(25) De Los Santos Valladares, L.; Salinas, D. H.; Dominguez, A. B.; Najarro, D. A.; Khondaker, S. I.; Mitrelias, T.; Barnes, C. H. W.; Aguiar, J. A.; Majima, Y. Crystallization and electrical resistivity of Cu_2O and CuO obtained by thermal oxidation of Cu thin films on SiO_2/Si substrates. *Thin Solid Films* **2012**, *520*, 6368−6374.
(26) Tang, Z.; Yeo, B. C.; Han, S. S.; Lee, T.-J.; Bhang, S. H.; Kim, W.-S.; Yu, T. Facile aqueous-phase synthesis of Ag−Cu−Pt−Pd quadrometallic nanoparticles. *Nano Convergence* **2019**, *6*, 38.
(27) Brundle, C. R.; Crist, B. V. X-ray photoelectron spectroscopy: A perspective on quantitation accuracy for composition analysis of homogeneous materials. *J. Vac. Sci. Technol., A* **2020**, *38*, No. 041001.
(28) Shi, Q.; Ping, G.; Wang, X.; Xu, H.; Li, J.; Cui, J.; Abroshan, H.; Ding, H.; Li, G. CuO/TiO_2 heterojunction composites: an efficient photocatalyst for selective oxidation of methanol to methyl formate. *J. Mater. Chem. A* **2019**, *7*, 2253−2260.
(29) Moniz, S. J. A.; Tang, J. Charge Transfer and Photocatalytic Activity in CuO/TiO_2 Nanoparticle Heterojunctions Synthesised through a Rapid, One-Pot, Microwave Solvothermal Route. *ChemCatChem* **2015**, *7*, 1659−1667.
(30) Choi, S.; Jeong, Y.; Yu, J. Spontaneous hydrolysis of borohydride required before its catalytic activation by metal nanoparticles. *Catal. Commun.* **2016**, *84*, 80−84.
(31) Sclafani, A.; Herrmann, J. M. Comparison of the Photoelectronic and Photocatalytic Activities of Various Anatase and Rutile Forms of Titania in Pure Liquid Organic Phases and in Aqueous Solutions. *J. Phys. Chem.* **1996**, *100*, 13655−13661.
(32) Tanaka, K.; Capule, M. F. V.; Hisanaga, T. Effect of crystallinity of TiO_2 on its photocatalytic action. *Chem. Phys. Lett.* **1991**, *187*, 73−76.
(33) Stafford, U.; Gray, K. A.; Kamat, P. V.; Varma, A. An in situ diffuse reflectance FTIR investigation of photocatalytic degradation of 4-chlorophenol on a TiO_2 powder surface. *Chem. Phys. Lett.* **1993**, *205*, 55−61.
(34) Aditya, T.; Pal, A.; Pal, T. Nitroarene reduction: a trusted model reaction to test nanoparticle catalysts. *Chem. Commun.* **2015**, *51*, 9410−9431.
(35) Pfeifer, V.; Erhart, P.; Li, S.; Rachut, K.; Morasch, J.; Brötz, J.; Reckers, P.; Mayer, T.; Rühle, S.; Zaban, A.; Mora Seró, I.; Bisquert, J.; Jaegermann, W.; Klein, A. Energy Band Alignment between Anatase and Rutile TiO_2. *J. Phys. Chem. Lett.* **2013**, *4*, 4182−4187.
(36) Yang, Q.; Beers, M. H.; Mehta, V.; Gao, T.; Parkinson, D. Effect of Thermal Annealing on the Electrical Conductivity of Copper−Tin Polymer Composites. *ACS Appl. Mater. Interfaces* **2017**, *9*, 958−964.
(37) Lv, X.-J.; Zhou, S.-X.; Zhang, C.; Chang, H.-X.; Chen, Y.; Fu, W.-F. Synergetic effect of Cu and graphene as cocatalyst on TiO_2 for enhanced photocatalytic hydrogen evolution from solar water splitting. *J. Mater. Chem.* **2012**, *22*, 18542−18549.
(38) Liu, J.; Wu, Q.; Huang, F.; Zhang, H.; Xu, S.; Huang, W.; Li, Z. Facile preparation of a variety of bimetallic dendrites with high catalytic activity by two simultaneous replacement reactions. *RSC Adv.* **2013**, *3*, 14312−14321.

https://doi.org/10.1021/acsomega.3c01285
ACS Omega 2023, 8, 17234−17244

(39) Zhao, F.; Kong, W.; Hu, Z.; Liu, J.; Zhao, Y.; Zhang, B. Tuning the performance of Pt−Ni alloy/reduced graphene oxide catalysts for 4-nitrophenol reduction. *RSC Adv.* **2016**, *6*, 79028−79036.
(40) Zhou, Y.; Zhu, Y.; Yang, X.; Huang, J.; Chen, W.; Lv, X.; Li, C.; Li, C. Au decorated Fe_3O_4@TiO_2 magnetic composites with visible light-assisted enhanced catalytic reduction of 4-nitrophenol. *RSC Adv.* **2015**, *5*, 50454−50461.
(41) Zhang, P.; Shao, C.; Zhang, Z.; Zhang, M.; Mu, J.; Guo, Z.; Liu, Y. In situ assembly of well-dispersed Ag nanoparticles (AgNPs) on electrospun carbon nanofibers (CNFs) for catalytic reduction of 4-nitrophenol. *Nanoscale* **2011**, *3*, 3357−3363.
(42) Miao, L.; Liu, G.; Wang, J. Ag-Nanoparticle-Bearing Poly(vinylidene fluoride) Nanofiber Mats as Janus Filters for Catalysis and Separation. *ACS Appl. Mater. Interfaces* **2019**, *11*, 7397−7404.
(43) Kohantorabi, M.; Gholami, M. R. Kinetic Analysis of the Reduction of 4-Nitrophenol Catalyzed by CeO_2 Nanorods-Supported CuNi Nanoparticles. *Ind. Eng. Chem. Res.* **2017**, *56*, 1159−1167.
(44) Tony, M. A.; Mansour, S. A. Removal of the commercial reactive dye Procion Blue MX-7RX from real textile wastewater using the synthesized Fe_2O_3 nanoparticles at different particle sizes as a source of Fenton's reagent. *Nanoscale Adva.* **2019**, *1*, 1362−1371.
(45) Mohamed, M. M.; Al-Sharif, M. S. Visible light assisted reduction of 4-nitrophenol to 4-aminophenol on Ag/TiO_2 photocatalysts synthesized by hybrid templates. *Appl. Catal., B* **2013**, *142-143*, 432−441.
(46) Nezamzadeh-Ejhieh, A.; Khorsandi, S. Photocatalytic degradation of 4-nitrophenol with ZnO supported nano-clinoptilolite zeolite. *J. Ind. Eng. Chem.* **2014**, *20*, 937−946.
(47) Mele, G.; Garcìa-Lòpez, E.; Palmisano, L.; Dyrda, G.; Słota, R. Photocatalytic Degradation of 4-Nitrophenol in Aqueous Suspension by Using Polycrystalline TiO_2 Impregnated with Lanthanide Double-Decker Phthalocyanine Complexes. *J. Phys. Chem. C* **2007**, *111*, 6581−6588.
(48) Kalarivalappil, V.; Divya, C. M.; Wunderlich, W.; Pillai, S. C.; Hinder, S. J.; Nageri, M.; Kumar, V.; Vijayan, B. K. Pd Loaded TiO_2 Nanotubes for the Effective Catalytic Reduction of p-Nitrophenol. *Catal. Lett.* **2016**, *146*, 474−482.
(49) Konar, S.; Kalita, H.; Puvvada, N.; Tantubay, S.; Mahto, M. K.; Biswas, S.; Pathak, A. Shape-dependent catalytic activity of CuO nanostructures. *J. Catal.* **2016**, *336*, 11−22.
(50) Chi, Y.; Yuan, Q.; Li, Y.; Tu, J.; Zhao, L.; Li, N.; Li, X. Synthesis of Fe_3O_4@SiO_2−Ag magnetic nanocomposite based on small-sized and highly dispersed silver nanoparticles for catalytic reduction of 4-nitrophenol. *J. Colloid Interface Sci.* **2012**, *383*, 96−102.

https://doi.org/10.1021/acsomega.3c01285
ACS Omega 2023, 8, 17234−17244